# Rapid Conjugate Appearance of the Giant Ionospheric Lamb Wave in the Northern Hemisphere After Hunga-Tonga Volcano Eruptions.

Jia-Ting Lin[1], Panthalingal K. Rajesh[1], Charles C. H. Lin[1], Min-Yang Chou[2, 3], Jann-Yenq Liu[4, 5], Jia Yue[2, 3], Tung-Yuan Hsiao[6], Ho-Fang Tsai[1], Hoi-Man Chao[1] and Mu-Min Kung[1]

[1] Department of Earth Sciences, National Cheng Kung University, Tainan, Taiwan

[2] NASA Goddard Space Flight Center, Community Coordinated Modeling Center, Greenbelt, MD, USA

[3] Physics Department, Catholic University of America, Washington, DC, USA

[4] Center for Astronautical Physics and Engineering, National Central University, Taiwan

[5] Department of Space Science and Engineer, National Central University, Taiwan

[6] Nuclear Science and Technology Development Center, National Tsing Hua University, Hsinchu, Taiwan

**Key points:**

1. Concentric traveling ionospheric disturbances (CTIDs) driven by volcano excited Lamb wave are observed simultaneously in Australia and Japan.

2. Due to instantaneous magnetic field conjugate effect, the northern hemisphere CTIDs appear 3-hours prior to the arrival of surface Lamb wave

3. The CTIDs from conjugate hemispheres match with the theoretical dispersion relation of the atmospheric Lamb mode.

**Abstract**

The explosive eruption of the Hunga-Tonga volcano in the southwest Pacific at 0415UT on 15 January 2022 triggered gigantic atmospheric disturbances with surface air pressure wave propagating around the globe in Lamb mode. In space, concentric traveling ionosphere disturbances (CTIDs) are also observed as a manifestation of air pressure acoustic waves in New Zealand ~0500UT and Australia ~0630UT. As soon as the wave reached central Australia ~0800UT, CTIDs appeared simultaneously in the northern hemispheres through magnetic field line conjugate effect, which is much earlier than the arrival of the air pressure wave to Japan after 1100UT. Combining observations over Australia and Japan between 0800-1000UT, CTIDs with characteristics of phase velocities of 320-390 m/s are observed, matching with the dispersion relation of Lamb mode. The arrival of atmospheric Lamb wave to Japan later created in situ CTIDs showing the same Lamb mode characteristics as the earlier arriving CTIDs.

## Plain Language Summary

The Hunga-Tonga Volcano eruption on 15 January 2022 has created the impulsive Lamb wave propagation on the surface air pressure that has been observed globally. The Lamb wave, typically moving at the sound speed of ~340 m/s, traveled 6 hours to reach Japan, but the Lamb wave signature in the Earth's ionosphere, the ionized component of the atmosphere, arrived 3-hours earlier than expected, thanks to the property of the ionospheric plasma being controlled by the Earth's magnetic field. As soon as the surface Lamb wave reached Australia, the ionosphere above showed concentric wave shape of the traveling ionospheric disturbances (TIDs) and the effect was mapped to the northern hemisphere through the conductive magnetic field lines. This is the first time such concentric waves from a volcanic eruption is observed simultaneously in both the hemispheres. The much faster transmission of the ionosphere disturbances to the northern hemisphere through the magnetic field lines is beyond expectations. Monitoring the ionospheric disturbances could be a powerful early warning tool for the diagnosis of such explosive events on the planet Earth.

## 1. Introduction

Although constrained along the magnetic field lines with gyro-motions, the plasma distribution in the ionosphere, the ionized component of the Earth's atmosphere, could be affected by perturbations in the neutral atmosphere through momentum transfer by ion-neutral collisions (e.g. Heki and Ping, 2005), or through polarization electric field perpendicular to magnetic field that drives $\delta E \times B$ electromagnetic drift across field lines (e.g. Chou et al., 2017a), given that neutrals are abundant than ions at the ionospheric altitudes. Thus, neutral atmospheric perturbations could be seen through the observations such as ionospheric total electron content (TEC), and one of the signature forms of this coupling is the generation of traveling ionospheric disturbances (TIDs). Such TIDs with shock acoustic characteristics occurred after rocket launches accompanied by atmospheric perturbations (Lin et al., 2014; 2017a; Chou et al., 2018a). Concentric TIDs (CTIDs), the feature of the concentric gravity wave effect to the ionosphere, are observed associated with extreme weather systems in the lower atmosphere (e.g. Nishioka et al., 2013; Chou et al., 2017b). There are events that created a broad spectrum of perturbations in both acoustic and gravity wave modes, e.g., rocket launches that produce shock-acoustic waves followed by concentric gravity waves (Lin et al., 2017b) or thermospheric ducted gravity waves (Chou et al., 2018b). An extreme case is the 2011 Tohoku earthquake and tsunami which triggered a diverse spectra of TIDs, including phase velocities of the high-speed Rayleigh wave mode of ~3.5 km/s, acoustic mode of 1-1.2 km/s, gravity mode of ~300-590 m/s and tsunami mode of ~200-250 m/s (e.g. Chen et al., 2011; Liu et al., 2011a; Rolland et al., 2011; Saito et al., 2011; Tsugawa et al., 2011; Galvan et al., 2012; Azeem et al., 2017; Chou et al., 2020).

Additionally, explosive volcano events that release elevated plume to the atmosphere could also produce TIDs (e.g. Heki, 2006), and most of the reported perturbations fall within the shock

and acoustic mode with frequencies of ~4-6 mHz. Shults et al. (2016) show that the eruption of the Calbuco volcano on 22-23 April 2015 generated acoustic wave in the ionosphere with the phase velocities of 900-1200 m/s. They also listed three other volcano events showing similar phase velocity in the acoustic wave domain (Heki, 2006; Dautermann et al., 2009a, 2009b; Nakashima et al., 2016). Nakashima et al. (2016) show TEC oscillations with frequencies of 3.7, 4.8 and 6.8 mHz, which are similar to the 4-6 mHz oscillations reported by Shults et al. (2016). While these ionospheric perturbations in the acoustic mode reported in the above events were limited within about 1000 km of the volcano source (Shults et al., 2016), one of the most significant events that induced global atmosphere responses was the eruption of St. Helen on 18 May 1980. Liu et al. (1982) showed that the eruption of St. Helen created atmospheric pressure disturbance waves and TIDs in the ionosphere worldwide. Their observations of TIDs could only be explained by the propagation of the atmospheric Lamb wave modes with horizontal phase velocity at the sound speed of ~310 m/s, with period ranging within 5-50 min.

Similar to the impacts reported during the St. Helen event, the recent Hunga Tonga - Hunga Ha‘apai volcano eruption on 15 January 2022, sent out bouts of shock waves rippling through the air, literally making the entire atmosphere to vibrate. The breathtaking images of the event captured by Earth observing satellites show Lamb waves circulating the Earth, with worldwide ground weather stations recording multiple passages of the air pressure waves (Duncombe, 2022). The atmospheric disturbances from this violent eruption triggered a plethora of wave perturbations, impacting the ocean surfaces and creating atmospheric oscillations, including acoustic and gravity waves (e.g. Adam, 2022) that could potentially modulate the electron content in the ionosphere. The TEC observations show CTID’s reaching several thousands of kilometers away from the eruption source. Taking advantage of the dense Global Navigation

Satellite System (GNSS) receiver network over New Zealand, Australia, and Japan, we image the Lamb wave perturbations in the ionosphere displaying CTIDs over Japan at least 3-hours ahead of the expected arrival of the disturbances based on the estimates of the air pressure wave propagation (according to the manuscript submitted at scientific online letters by Sekizawa and Kohyama 2022; https://doi.org/10.31223/X55K8V, hereinafter referred to as Sekizawa and Kohyama, 2022). This shows intriguing coupling from the magnetic conjugate regions in the southern hemisphere. Chou et al. (2022) recently showed conjugate signatures of medium scale traveling ionosphere disturbances (MSTID) produced by the tsunami propagation during the 2011 Tohoku earthquake. However, this is the first time such conjugate behavior of ionosphere dynamo in coupling the polarization electric fields associated with concentric gravity waves produced by the atmospheric perturbations from a volcanic eruption is observed. The wave characteristics of the observed CTIDs and their conjugate appearances are discussed.

## 2. GNSS TEC Observations

The Hunga Tonga - Hunga Ha‘apai islands (20.5S, 175.8 E) are rightly placed in the proximity of the GNSS network maintained by Geological hazard information for New Zealand and Geoscience Australia, offering the opportunity to examine the near filed impact from the volcanic eruption. Both the services combined adds up to about 600 GNSS receivers, receiving signals from Global Positioning System (GPS) and GLObal Navigation Satellite System (GLONASS) satellites. In addition, data from about 1300 stations of the GNSS network of the Geospatial Information Authority of Japan and 140 stations of Central Weather Bureau of Taiwan (Shin et al., 2011; 2013) are also used. Such dense networks, though limited to certain regions, enables rapid examination of TEC variations with high spatial and temporal resolutions.

The information about the data sources is given in the Open Research section. The 30-second sampled GNSS observations are used to derive vertical TEC at a sub-ionospheric altitude of 300 km, with a low elevation cut-off of 20°. The TEC variations are extracted by applying Butterworth bandpass filters of 12-20 mins and 30-50 min to better present the small- and large-scale atmospheric waves associated with the volcanic eruption before distributing to their geolocations of the sub-ionospheric points (SIPs).

Figure 1 shows the time evolution of the filtered TEC maps for periods within 30-50 mins and 12-20 mins at 0647, 0853, 0926 and 1120 UT. The filtered TECs projected to the conjugated hemisphere using magnetic apex coordinates (Richmond, 1995; Emmert et al., 2010) are also shown using different colormaps. Overplotted red dashed circles indicate the atmospheric disturbances, mostly the Lamb wave, traveling at the speed of sound calculated using temperature from NCEP reanalysis (Kalnay et al., 1998) and mean molecular mass from the empirical NRLMSISE-00 model (Picone et al., 2002). According to Sekizawa and Kohyama (2022), the arrival of the air pressure disturbances at Japan is ~1100UT and the estimation indicated by the dashed circles matches the arrival time. Liu et al. (1982) show from their model calculation that the TIDs of acoustic-gravity waves associated with lamb modes are ~5-50 mins and we, therefore, focus on the TEC oscillations within these time periods. The bandpass filtering is performed at 12-20 min (hereinafter referred as 12-20 wave) to illustrate the finer structure of the CTIDs and at 30-50 min (hereinafter referred as 30-50 wave) to show the larger scale CTIDs. The movie of the time evolutions of bandpass filtering of 12-20, 30-50 and 10-60 mins are provided in the supplementary material (Movie S1). In Figure 1 and movie S1, CTIDs of both bands are seen clearly over New Zealand and Australia area after 0647UT and become prominent and clearly conjugated, either mapping the Australia TECs to the northern hemisphere

or mapping the Japan TECs to the southern hemisphere after 0800UT. Thirty minutes ahead of the arrival of the surface pressure wave in Japan, around 1030 UT, the propagation direction of CTIDs in Japan started to turn from westward to north-westward, aligning perpendicular to the wavefront of the surface waves. The 12-20 waves start to show direction change of the wavefront ~1045UT, lagging ~15 minutes behind the 30-50 waves. The clear conjugated waves are still seen in the southern hemisphere for the 12-20 wave after 1100UT upon the direct arrival of the surface wave to Japan.

The spectral analysis of the GNSS TEC from both Australia and Japan has been performed for oscillations of periods shorter than 1 h by using Hilbert-Huang transform (HHT, cf. Huang et al., 1998; Liu et al., 2011b). Note that only TEC observations over the conjugate area (130-140°E) are used to investigate the ionospheric conjugacy of CTIDs. Figure 2 shows the Hilbert spectrum of TECs from both Australia and Japan. The amplitudes of both Hilbert spectra start to intensify coherently ~0700UT and become prominent around 0800-1000UT, peaking at ~0900UT for both regions for periods greater than 10 mins. Generally, the amplitude intensifications occur after 0700UT for both spectra in the frequency range ~0.25-2 mHz or period of 8-60 min, which is consistent with the 5-50 mins period suggested by Liu et al. (1982).

Figure 3 illustrate the keograms of the filtered TECs of New Zealand and Australia (Figs. 3a, c) and Japan (Fig. 3b, d). As the filtered TECs over Japan are mapped to the southern hemisphere, the distances to the volcano are counted from their southern hemisphere magnetic conjugate locations. Figure 3a shows, for the 30-50 min period, that the first prominent packet of TIDs appears clearly over New Zealand (distances < 3000 km) around 0500-0700UT. The second prominent packet appears over Australia ~0700-1000UT. The 12-20 waves (Fig. 3c) lag behind

30-50 waves for at least 15 min or even longer. Clear conjugate effects for the two periods are seen in the TIDs over Japan after 0730UT (Figs. 3c and 3d).

Except TID#NZ1, which shows phase velocity exceeding 500 m/s, most of the TIDs have phase velocities of 320-390 m/s, and periods of ~40 mins for the 30-50 waves and 15-18 mins for the 12-20 waves. These wave characteristics are further applied to estimate the dispersion relation using Equation (1) (cf. Hines, 1960) expressed as follows. The equation is also utilized to calculate the dispersion curves of acoustic and gravity modes.

$$m^2 = \left(1 - \frac{\omega_a^2}{\omega^2}\right)\frac{\omega^2}{{c_0}^2} - k^2\left(1 - \frac{\omega_b^2}{\omega^2}\right) \quad (1)$$

where m is the complex vertical wave number, $\omega_a = \sqrt{\frac{\gamma g}{4H} + \frac{g}{T}\frac{dT}{dz}}$ is acoustic cutoff frequency, $\omega_b = \sqrt{\frac{(\gamma-1)g}{\gamma H} + \frac{g}{T}\frac{dT}{dz}}$ is buoyancy frequency, $\omega = k(c_h - u)$ is intrinsic frequency, u is the neutral wind speed in the direction of wave propagation, $c_h$ is the horizontal phase velocity, H is the scale height, γ is the ratio of specific heats, $g$ is the gravitational acceleration, and T is neutral temperature. These parameters are adopted from empirical neutral atmospheric parameters from the Horizontal Wind Model 2014 (Drob et al., 2015) and NRLMSISE-00. The acoustic-gravity wave is evanescent or freely propagating while $m^2<0$ or $m^2>0$. We identify the characteristic of these TIDs by calculating the dispersion curves for Figure 4 ($m^2 = 0$) using equation (1) (cf. Yeh and Liu, 1974; Matsumura et al., 2012). The black solid, dashed, dashed-dot and dotted lines indicate the dispersion curves of gravity mode and acoustic mode at 300, 250, 200 and 150 km altitude, respectively. The colored dots indicate the calculated intrinsic frequencies of observed TIDs indicated in Figure 3. The Lamb wave mode with constant phase velocity of sound is added

with the blue solid line in Figure 4. It is seen that the color dots of TIDs are aligned along the blue solid line indicating the Lamb wave signature of CTIDs observed in this study.

Since atmospheric Lamb wave has non-dispersive characteristics as acoustic waves (Francis, 1973), it is expected to see similar wave characteristics of CTIDs over Japan after the actual arrival of the Lamb wave to Japan ~1100UT. Figure S2 shows the 30-50 and 12-20 waves over Japan ~1000-1400UT. It indicates that the 30-50 waves again lead the 12-20 wave, and these waves generally fit along the curve of Lamb mode, except the early appearance of 12-20 waves (TID#JP6, JP7 and JP8).

## 3. Discussions and Conclusion

We present the first clear images of CTIDs propagating with the Lamb mode driven by the volcano excited Lamb wave for the first time (Fig. 1). Taking advantage of the magnetic conjugate effect by combining observations from Australia and Japan, a comprehensive picture of concentric waves could be drawn, and their wave characteristics are all consistent with the dispersion relation of Lamb mode as shown in Figs. 3 and 4. Another important discovery is that the CTIDs could be seen conjugately even during daytime (Dusk), which was not previously reported in the literature. This new finding suggests that the Lamb wave excited by the explosive Hunga Tonga - Hunga Ha‘apai volcano could affect the global ionosphere much sooner than expected as the driven CTIDs are capable of being transmitted to the magnetically conjugate hemispheres.

During the geomagnetically quiescent period, the magnetic conjugate effect of the ionosphere is well known and there are studies on the conjugate effect of plasma instabilities during nighttime, such as equatorial plasma bubble (EPB) and MSTID (e.g. Otsuka et al., 2004;

Fukushima et al., 2015; Valladares and R. Sheehan, 2016). During daytime the conjugate effect is believed to be rare because the efficiency of electric field mapping is proportional to the ratio of field line integration of the Pedersen conductivities in F- and E-regions as $\frac{\Sigma_p^F}{\Sigma_p^F+\Sigma_p^E}$. The much higher E-region conductivity during daytime then prevents the electric field mapping in the F-region. However, some exceptions were observed by Jonah et al. (2017) and they adopted the explanation given by Abdu et al. (2015) that during the late afternoon approaching the sunset hours, the ratio of F- and E-region conductivities could be close to 0.8 or greater making electric field mapping likely to happen. Our observation of the Lamb wave driven CTIDs in Japan appeared after 0730UT or 1630LT, close to the time-period when the mapping is likely favored.

The 2011 Great Tohoku earthquake and tsunami also triggered conjugate effect of the tsunami driven gravity waves, but they were mainly during nighttime. Huba et al. (2015) simulated the conjugate ionospheric effects associated with the tsunami-driven gravity waves using self-consistent electrodynamics and suggested that the perpendicular neutral wind perturbation could induce polarization electric fields mapping along the geomagnetic field line to the conjugate southern hemisphere of Hawaii. Their simulations were compared with the sparse GPS-derived TEC when the tsunami passed by Hawaii during nighttime. Chou et al. (2022) discovered that the reflected tsunami was able to drive gravity waves over Japan and triggered prominent MSTID occurring in March, a season of rare MSTID occurrence, and further mapped to the conjugate southern hemisphere over Australia. However, the initial main TIDs driven by the earthquake and tsunami did not produce any conjugate effect, and the coupled gravity wave-Perkins instability may contribute to the interhemispheric conjugate process due to the specific wavefront alignment of the MSTIDs. This study, therefore, provides direct observational

evidence to support that wind-dynamo coupling (e.g., Huba et al., 2015) alone is sufficient to induce the conjugate effect.

Surface air pressure wave traveling with Lamb mode occurred during previous explosion events, e.g. Kratatoa volcano eruption in 1883 (Pekeries, 1939), Tunguska event in Siberia 1908 (Whippe, 1930) and St. Helen eruption in 1980 (Liu et al., 1980). According to Francis (1973), the lower atmosphere Lamb wave could propagate long distances with little dissipation and its attenuation distance, defined by attenuation by a factor of 1/e, is of the order of Earth's circumference or greater. The non-dispersive and weak attenuation properties of the air pressure wave (Duncombe, 2022) again suggest that it is the Lamb wave traveling globally, excited by the volcano eruption, being studied here. The ionosphere disturbances also show weak attenuation feature. The amplitudes of the CTIDs (percentage of TEC perturbations) over New Zealand-Australia around 0500-1000UT (Figs. 3a and 3b) and Japan, more than 8000 km away from the volcano, around 1000-1300UT, are comparable (Fig S2), indicating the weak attenuation nature of the Lamb wave. Although the Lamb wave generally travels in the troposphere and stratosphere below about 30 km altitude and its energy decreases with altitudes, the exponential decrease of neutral density with increasing altitude actually increases its amplitude. Additionally, Nishida et al. (2014) show that Lamb wave could theoretically exist at thermosphere altitudes. Our observations of CTIDs agree with the dispersion relation of Lamb mode and the weak attenuation suggests that the CTIDs driven by the Hunga-Tonga volcano have Lamb wave characteristics.

It is worthwhile to note that (according to Fig. 1 and Movie S1), prior to the arrival of the air pressure Lamb wave to Australia, there are already signatures of TIDs. By comparing with the intense tsunami effect of the 2011 Tohoku earthquake, there were leading TIDs ahead of the

tsunami arrival (e.g. Makela et al., 2011). Inchin et al. (2020) suggest that the tsunami-induced gravity wave spectrum has phase variations from long-period phases at the head of the packet to short-period phases at its tail. A similar process might occur in this event, where, instead of the tsunami exciting the gravity waves the surface Lamb wave might excite a broad spectrum of gravity waves. Gravity waves with longer period waves travel faster than short period waves (Figs. 1, 3, S2). Gravity waves with the period locked to the dominant period of Lamb mode will eventually travel at the same speed of surface pressure wave after reaching the ionosphere and the surface pressure Lamb wave plays the role of continuously triggering gravity wave as a moving source. This process is also similar to the seismic Rayleigh wave that continuously excites seismo-TIDs with the same periods and speeds (e.g., Liu et al., 2011a).

Rakoto et al. (2017) developed the ocean-atmosphere coupled model for tsunami effects with analyses of acoustic, gravity, tsunami and Lamb modes. They find that the tsunami mode does not transfer energy to the Lamb mode through resonance as their frequency branches are not crossing each other. On the other hand, the tsunami mode could excite gravity waves due to the crossing frequency branches of the tsunami and gravity modes. Similarly, for the volcano effect discussed here, the Lamb mode frequency crosses through the frequencies of gravity modes (Figs. 4 and S3) and it is likely that the Lamb wave could thereby induce a packet of gravity waves. The lagged 12-20 waves in Fig. 1 and the keograms of Figs. 3 and S2 showing the smaller scale waves appearing at later times suggest that such a process might be operational.

It is noted that there was a minor magnetic storm during the volcano eruption, with the disturbance storm index (Dst) dropping to about -94 nT at ~2300 UT on 14 January 2022. Magnetic storms are known to generate large-scale TIDs (LSTIDs) that propagate equatorward (e.g., Richmond, 1978), and could give rise to TEC perturbations (Cherniak and Zakharenkova,

2018). However, the storm influence could be ruled out here to have any role in producing the TEC observed fluctuations after the eruption. Though interplanetary magnetic field (IMF Bz) turned southward after 1800 UT on this day, gradually reaching about -18 nT by 2230 UT, the solar wind velocity was only 350-380 km/s during this period and the proton density did not increase much, suggesting only minor storm impact. The auroral electrojet (AE) index, which briefly reached over 1000 during 2100-2200 UT, and again spiked for a few minutes before 2300 UT on 01/14 when IMF Bz was southward, returned to values below 500 before 0000 UT on 01/15 and subsequently remained subdued, further indicating lack of any significant high latitude activity. The IMF Bz also turned northward by 2330 UT on 01/14, and later revealed fluctuations typical of CIR events. The Dst index further shows that by the time the eruption occurred, the storm was well into the recovery phase. Moreover, LSTIDs usually propagate equatorward from high latitudes, whereas the observed perturbations show CTIDs expanding poleward as the Lamb waves circulated the Earth.

In conclusion, we present the first comprehensive picture of the concentric traveling ionospheric disturbances in conjugate hemispheres coherently showing the Lamb wave characteristic driven by the powerful eruption of Hunga Tonga - Hunga Ha‘apai. The varying phase velocities of the ionospheric disturbances with different wave periods suggest that the Lamb waves excite a broad spectra of gravity waves, further indicating resonant wave-coupling of co-existing Lamb and gravity modes. The conductive geomagnetic field lines enable the rapid transmission of disturbance waves to the northern hemisphere on Alfvénic timescales (~300 km/s), leading to rapid electrified ionospheric disturbances faster than the direct Lamb waves over Japan, which is beyond expectations. The GNSS networks therefore could be a powerful

tool for early warning system for the diagnosis of such explosive events on the planet Earth, and advance our understanding of how natural hazards drive space weather.

**Acknowledgements**

This work is partly supported by the Ministry of Science and Technology under MOST 110-2111-M-006-004 and MOST 110-2119-M-006-001. MYC was supported by NASA grant 80NSSC20K0628. CHL wishes to thank Chao-Han Liu for useful discussions. The authors acknowledge the Geological hazard information for New Zealand, the Geoscience Australia, the Geospatial Information Authority of Japan, the Central Weather Bureau, Taiwan for managing the GNNS observations, and the Geomagnetic Data Service of Kyoto University and NOAA Space Weather Prediction Center for geomagnetic and solar wind parameters.

**Open Research**

The GNSS RINEX data are available from the Geological hazard information for New Zealand (GeoNet, https://www.geonet.org.nz/data/types/geodetic), the Geoscience Australia GNSS data archive (https://www.ga.gov.au/scientific-topics/positioning-navigation/geodesy/gnss-networks), the Geospatial Information Authority of Japan (GEONET, https://www.gsi.go.jp/ENGLISH/geonet_english.html) and the Geophysical Database Management System of Central Weather Bureau, Taiwan (https://gdms.cwb.gov.tw/index.php). Dst and AE indices are available at the Geomagnetic Data Service of Kyoto University (http://wdc.kugi.kyoto-u.ac.jp/wdc/Sec3.html) and the solar wind parameters could be accessed from NOAA Space Weather Prediction Center (https://www.swpc.noaa.gov/products/real-time-

318 solar-wind). The processed TEC data is available at
319 https://doi.org/10.6084/m9.figshare.19115624.

320

321 **Reference**


322 Abdu, M. A., J. R. de Souza, E. A. Kherani, I. S. Batista, J. W. MacDougall, and J. H. A. Sobral
323 (2015), Wave structure and polarization electric field development in the bottomside F
324 layer leading to postsunset equatorial spread F, J. Geophys. Res. Space Physics, 120,
325 6930–6940, doi:10.1002/2015JA021235.

326 Adam, D. (2022), Tonga volcano eruption created puzzling ripples in Earth's atmosphere,
327 *Nature* **601**, 497.

328 Azeem, I., Vadas, S. L., Crowley, G., and Makela, J. J. (2017), Traveling ionospheric
329 disturbances over the United States induced by gravity waves from the 2011 Tohoku
330 tsunami and comparison with gravity wave dissipative theory, J. Geophys. Res. Space
331 Physics, 122, 3430– 3447, doi:10.1002/2016JA023659.

332 Chen, C. H., A. Saito, C. H. Lin, J. Y. Liu, H. F. Tsai, T. Tsugawa, Y. Otsuka, M. Nishioka and
333 M. Matsumura (2011), Long-distance propagation of ionospheric disturbance generated by
334 the 2011 Tohoku earthquake, Earth Planets and Space, 63, 7, 881-884,
335 doi:10.5047/eps.2011.06.026

336 Cherniak, I., and Zakharenkova, I. (2018). Large-scale traveling ionospheric disturbances origin
337 and propagation: Case study of the December 2015 geomagnetic storm. Space Weather, 16,
338 1377– 1395. https://doi-org.cuucar.idm.oclc.org/10.1029/2018SW001869

339 Chou, M. Y., C. H. Lin, J. Yue, L. C. Chang, H. F. Tsai and C. H. Chen (2017a), Medium-scale
340 traveling ionospheric disturbances triggered by Super Typhoon Nepartak (2016), Geophys.
341 Res. Lett., 44, 7569–7577, doi:10.1002/2017GL073961
342 Chou, M. Y., C. H. Lin, J. Yue, H. F. Tsai, Y. Y. Sun, J. Y. Liu and C. H. Chen (2017b),
343 Concentric traveling ionosphere disturbances triggered by Super Typhoon Meranti (2016),
344 *Geophys. Res. Lett.*, 44, doi:10.1002/2016GL072205.
345 Chou, M. Y., M. H. Shen, C. H. Lin, J. Yue, C. H. Chen, J. Y. Liu and J. T. Lin (2018a),
346 Gigantic circular shock acoustic waves in the ionosphere triggered by the launch of
347 FORMOSAT-5 satellite, *Space Weather*, 16, 172-184, doi:10.1002/2017SW001738.
348 Chou, M.-Y., Lin, C. H., Shen, M.-H., Yue, J., Huba, J. D., & Chen, C.-H. (2018b), Ionospheric
349 disturbances triggered by SpaceX Falcon Heavy ,*Geophysical Research*
350 *Letters*, 45, doi:10.1029/2018GL078088.
351 Chou, M.-Y., Cherniak, I., Lin, C. C. H., & Pedatella, N. M. (2020). The persistent ionospheric
352 responses over Japan after the impact of the 2011 Tohoku earthquake. Space Weather, 18,
353 e2019SW002302. https://doi.org/10.1029/2019SW002302
354 Chou, M.-Y., Yue, J., Lin, C. C. H., Rajesh, P. K., & Pedatella, N. M. (2022). Conjugate effect
355 of the 2011 Tohoku reflected tsunami-driven gravity waves in the ionosphere. *Geophysical*
356 *Research Letters*, 49, e2021GL097170, doi:10.1029/2021GL097170.
357 Dautermann, T., Calais, E., Lognonné, P., Mattioli, G.S., 2009a. Lithosphere– atmosphere–
358 ionosphere coupling after the 2003 explosive eruption of the Soufriere Hills Volcano,
359 Montserrat. Geophys. J. Int. 179 (3), 1537–1546.
360 Dautermann, T., Calais, E., Mattioli, G.S., 2009b. Global positioning system detection and
361 energy estimation of the ionospheric wave caused by the 13 July 2003 ex- plosion of the

Soufrière Hills Volcano, Montserrat. J. Geophys. Res. 114 (B2), B02202. doi:10.1029/2008JB005722.

Drob, D. P., Emmert, J. T., Meriwether, J. W., Makela, J. J., Doornbos, E., Conde, M., et al. (2015). An update to the horizontal wind model (HWM):The quiet time thermosphere. Earth Space Science, 2(7), 301–319. https://doi.org/10.1002/2014EA000089

Duncombe, J. (2022), The surprising reach of Tonga's giant atmospheric waves, Eos, 103, https://doi.org/10.1029/2022EO220050.

Emmert, J. T., A. D. Richmond, and D. P. Drob (2010), A computationally compact representation of Magnetic-Apex and Quasi-Dipole coordinates with smooth base vectors, J. Geophys. Res., 115(A8), A08322, doi:10.1029/2010JA015326.

Francis, S. H. (1973), Acoustic-gravity modes and large-scale traveling ionospheric disturbances of a realistic, dissipative atmosphere, *J. Geophys. Res.*, 78( 13), 2278– 2301, doi:10.1029/JA078i013p02278.

Fukushima, D., Shiokawa, K., Otsuka, Y., Nishioka, M., Kubota, M., Tsugawa, T., Nagatsuma, T., Komonjinda, S., and Yatini, C. Y. (2015), Geomagnetically conjugate observation of plasma bubbles and thermospheric neutral winds at low latitudes. *J. Geophys. Res. Space Physics*, 120, 2222– 2231. doi: 10.1002/2014JA020398.

Galvan, D. A., Komjathy, A., Hickey, M. P., Stephens, P., Snively, J., Tony Song, Y., Butala, M. D., and Mannucci, A. J. (2012), Ionospheric signatures of Tohoku-Oki tsunami of March 11, 2011: Model comparisons near the epicenter, *Radio Sci.*, 47, RS4003, doi:10.1029/2012RS005023.

383 Heki, K., and J. Ping (2005), Directivity and apparent velocity of the coseismic ionospheric
384 disturbances observed with a dense GPS array, *Earth Planet. Sci. Lett*., 236, 845–855,
385 doi:10.1016/j.epsl.2005.06.010.
386 Heki, K. (2006), Explosion energy of the 2004 eruption of the Asama Volcano, central Japan,
387 inferred from ionospheric disturbances, Geophys. Res. Lett., 33, L14303,
388 doi:10.1029/2006GL026249.
389 Hines, C. O. (1960), Internal atmospheric gravity waves at ionospheric heights, *Can. J. Phys.*, 38,
390 1441.
391 Huang, N. E., et al. (1998), The empirical mode decomposition and the Hilbert spectrum for
392 nonlinear and nonstationary time series analysis, Proc. R. Soc. London, Ser. A, 454, 903–
393 995, doi:10.1098/rspa.1998.0193.
394 Huba, J. D., G. Joyce, and J. Krall (2008), Three-dimensional equatorial spread F modeling,
395 Geophys. Res. Lett., 35, L10102, doi:10.1029/2008GL033509.
396 Huba, J. D., D. P. Drob, T.-W. Wu, andJ. J. Makela (2015), Modeling the ionospheric impact of
397 tsunami-driven gravity waves with SAMI3: Conjugate effects, Geophys. Res. Lett., 42,
398 5719–5726,doi:10.1002/2015GL064871.
399 Inchin, P. A., Heale, C. J., Snively, J. B., & Zettergren, M. D. (2020). The dynamics of nonlinear
400 atmospheric acoustic-gravity waves generated by tsunamis over realistic bathymetry.
401 Journal of Geophysical Research: Space Physics, 125, e2020JA028309.
402 https://doi.org/10.1029/2020JA028309
403 Jonah, O. F., E. A. Kherani, and E. R. De Paula (2017), Investigations of conjugate MSTIDS
404 over the Brazilian sector during daytime, J. Geophys. Res. Space Physics, 122, 9576–9587,
405 doi:10.1002/2017JA024365.

406 Kalnay, E., Kanamitsu, M., Kistler, R., Collins, W., Deaven, D., Gandin, L., Iredell, M., Saha,
407 S., White, G., Woollen, J., Zhu, Y., Chelliah, M., Ebisuzaki, W., Higgins, W., Janowiak, J.,
408 Mo, K. C., Ropelewski, C., Wang, J., Leetmaa, A., Reynolds, R., Jenne, R., & Joseph, D.
409 (1996). The NCEP/NCAR 40-Year Reanalysis Project, Bulletin of the American
410 Meteorological Society, 77(3), 437-472. Retrieved Feb 6, 2022, from
411 https://journals.ametsoc.org/view/journals/bams/77/3/1520-
412 0477_1996_077_0437_tnyrp_2_0_co_2.xml
413 Lin, C. H., Lin, J. T. Lin, C. H. Chen, M. Matsumura, J. Y. Liu, Y. Y. Sun, W. H. Chen, Y.
414 Kakinami, H. Liu, and R. J. Rau (2014), Ionospheric Shock Waves Triggered by Rockets,
415 *Ann. Geophys*., 32, 9, 1145–1152, doi:10.5194/angeo-32-1145-2014
416 Lin, C. H. , C. H. Chen, M. Matsumura, J.-T. Lin and Y. Kakinami (2017a), Observation and
417 simulation of the ionospheric disturbance waves triggered by rocket exhausts, *J. Geophys.*
418 *Res. Space Physics*, *122*, doi:10.1002/2017JA023951.
419 Lin, C. H., M. H. Shen, M. Y. Chou, C. H. Chen, J. Yue, P. C. Chen, and M. Matsumura (2017b),
420 Concentric traveling ionospheric disturbances triggered by the launch of a SpaceX Falcon
421 9 rocket, *Geophys. Res. Lett*., 44, 7578–7586, doi:10.1002/2017GL074192.
422 Liu, C. H., et al. (1982), Global dynamic responses of the atmosphere to the eruption of Mount
423 St. Helens on May 18, 1980, *J. Geophys. Res.*, 87( A8), 6281– 6290,
424 doi:10.1029/JA087iA08p06281.
425 Liu, J.-Y., C.-H. Chen, C.-H. Lin, H.-F. Tsai, C.-H. Chen, and M. Kamogawa (2011a),
426 Ionospheric disturbances triggered by the 11 March 2011 M9.0 Tohoku earthquake, J.
427 Geophys. Res., 116, A06319, doi:10.1029/2011JA016761.

Liu, J. Y., Y. Y. Sun, Y. Kakinami, C. H. Chen, C. H. Lin, and H. F. Tsai (2011b), Bow and stern waves triggered by the Moon's shadow boat, Geophys. Res. Lett., 38, L17109, doi:10.1029/2011GL048805.

Makela, J. J., et al. (2011), Imaging and modeling the ionospheric airglow response over Hawaii to the tsunami generated by the Tohoku earthquake of 11 March 2011, *Geophys. Res. Lett.*, *38*, L00G02, doi:10.1029/2011GL047860.

Matsumura, M., H. Shinagawa, and T. Iyemori (2012), Horizontal extension of acoustic resonance between the ground and the lower thermosphere, J. Atmos. Sol. Terr. Phys., 75-76, 127–132.

Nakashima, Y., K. Heki, A. Takeo, M. N. Cahyadi, A. Aditiya, and K. Yoshizawa (2016), Atmospheric resonant oscillations by the 2014 eruption of the Kelud volcano, Indonesia, observed with the ionospheric total electron contents and seismic signals, Earth Planet. Sci. Lett., 434, 112–116, doi:10.1016/j.epsl.2015.11.029.

Nishida, K., N. Kobayashi and Y. Fukao (2014), Background Lamb waves in the Earth's atmosphere, Geophys. J. Int., 196, 312–316, doi: 10.1093/gji/ggt413

Otsuka, Y., K. Shiokawa, T. Ogawa, and P. Wilkinson (2004), Geomagnetic conjugate observations of medium-scale traveling ionospheric disturbances at midlatitude using all-sky airglow imagers, Geophys. Res. Lett., 31, L15803, doi:10.1029/2004GL020262.

Pekeris, C. L. (1939), The propagation of a pulse in the atmosphere, Proc. R. Soc. London Ser. A, A171, 434-449.

Picone, J. M., A. E. Hedin, D. P. Drob, and A. C. Aikin (2002), NRLMSISE-00 empirical model of the atmosphere: Statistical comparisons and scientific issues, J. Geophys. Res., 107 (A12), 1468, doi:10.1029/2002JA009430.

Rakoto, V., P. Lognonné, L. Rolland (2017), Tsunami modeling with solid Earth–ocean–atmosphere coupled normal modes, Geophysical Journal International, Oxford University Press (OUP), 2017, 211 (2), pp.1119 - 1138. 10.1093/gji/ggx322 . hal-01737686

Richmond, A. D. (1978), Gravity wave generation, propagation, and dissipation in the thermosphere, J. Geophys. Res., 83(A9), 4131– 4145, doi:10.1029/JA083iA09p04131.

Richmond, A. D.**,** Ionospheric electrodynamics using Magnetic Apex Coordinates, *J. Geomagn. Geoelectr.*, *47*, 191–212, 1995.

Rolland, L.M., Lognonné, P., Astafyeva, E. *et al.* The resonant response of the ionosphere imaged after the 2011 off the Pacific coast of Tohoku Earthquake. *Earth Planet Sp* **63,** 62 (2011). https://doi.org/10.5047/eps.2011.06.020

Saito, A., Tsugawa, T., Otsuka, Y., Nishioka, M., Iyemori, T., Matsumura, M., Saito, S., Chen, C.H., Goi, Y., Choosakul, N., 2011. Acoustic resonance and plasma de- pletion detected by GPS total electron content observation after the 2011 off the Pacific coast of Tohoku Earthquake. Earth Planets Space 63 (7), 863–867, doi:10.5047/eps.2011.06.034.

Shin, T. C., K. W. Kuo, P. L. Leu, C. H. Tsai, and J. S. Jiang, 2011: Continuous CWB GPS array in Taiwan and applications to monitoring seismic activity. Terr. Atmos. Ocean. Sci., 22, 521-533, doi: 10.3319/TAO.2011.05.18.01(T)

Shin, T. C., C. H. Chang, H. C. Pu*, H. W. Lin, and P. L. Leu, 2013: The Geophysical Database Management System in Taiwan. Terr. Atmos. Ocean. Sci., 24, 11-18, doi: 10.3319/TAO.2012.09.20.01(T)

Shults, K., E. Astafyeva, and S. Adourian (2016), Ionospheric detection and localization of volcano eruptions on the example of the April 2015 Calbuco events, J. Geophys. Res. Space Physics, 121, 10,303–10,315, doi:10.1002/2016JA023382.)

474 Tsugawa, T., A. Saito, Y. Otsuka, M. Nishioka, T. Maruyama, H. Kato, T. Nagatsuma, and K. T.
475 Murata, Ionospheric disturbances detected by GPS total electron content observation after
476 the 2011 off the Pacific coast of Tohoku Earthquake, *Earth Planets Space*, **63**, this issue,
477 875–879, 2011.
478 Valladares, C. E., and R. Sheehan (2016), Observations of conjugate MSTIDs using networks of
479 GPS receivers in the American sector, Radio Sci., 51, 1470–1488,
480 doi:10.1002/2016RS005967.
481 Whipple, F. J. W. (1930), The great siberian meteor and the waves, seismic and aerial, which it
482 produced, Q. J. R. Meteorol. Soc., 56, 278-304.
483
484 Yeh, K. C., & Liu, C. H. (1974). Acoustic–gravity waves in the upper atmosphere. Reviews of
485 Geophysics, 12(2), 193–216.

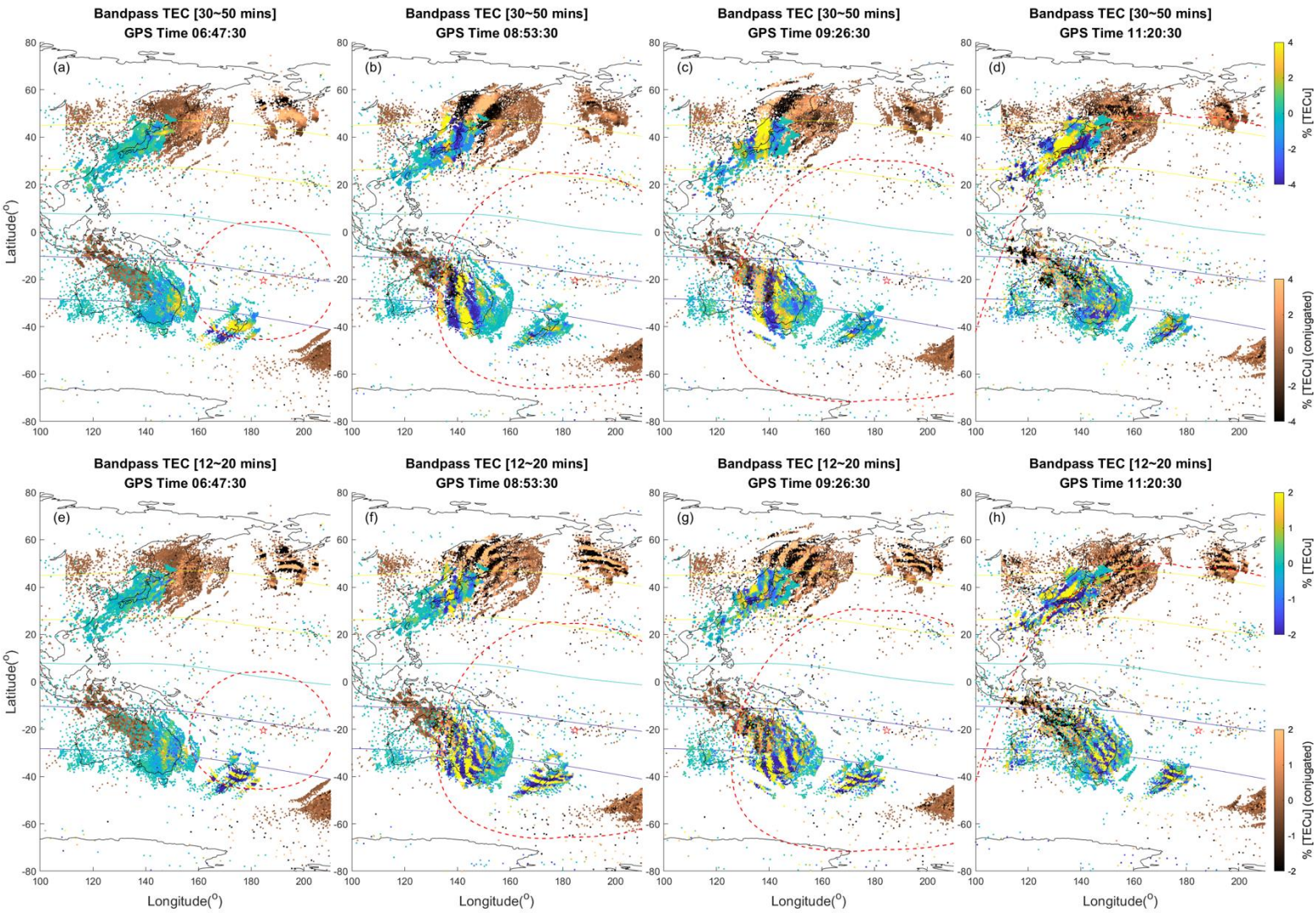


Figure 1. (a)-(d) Bandpass filtered TECs of 30-50 min periods showing the conjugate concentric TIDs after mapping Japan (Australia) TECs to Sothern (Northern hemisphere), (e)-(h) with bandpass filter of 12-20 min. The original TECs are plotted with "parula" colormap consisting of blue, green and yellow, while the conjugate TECs are plotted with "copper" colormap consisting of black and gold color.

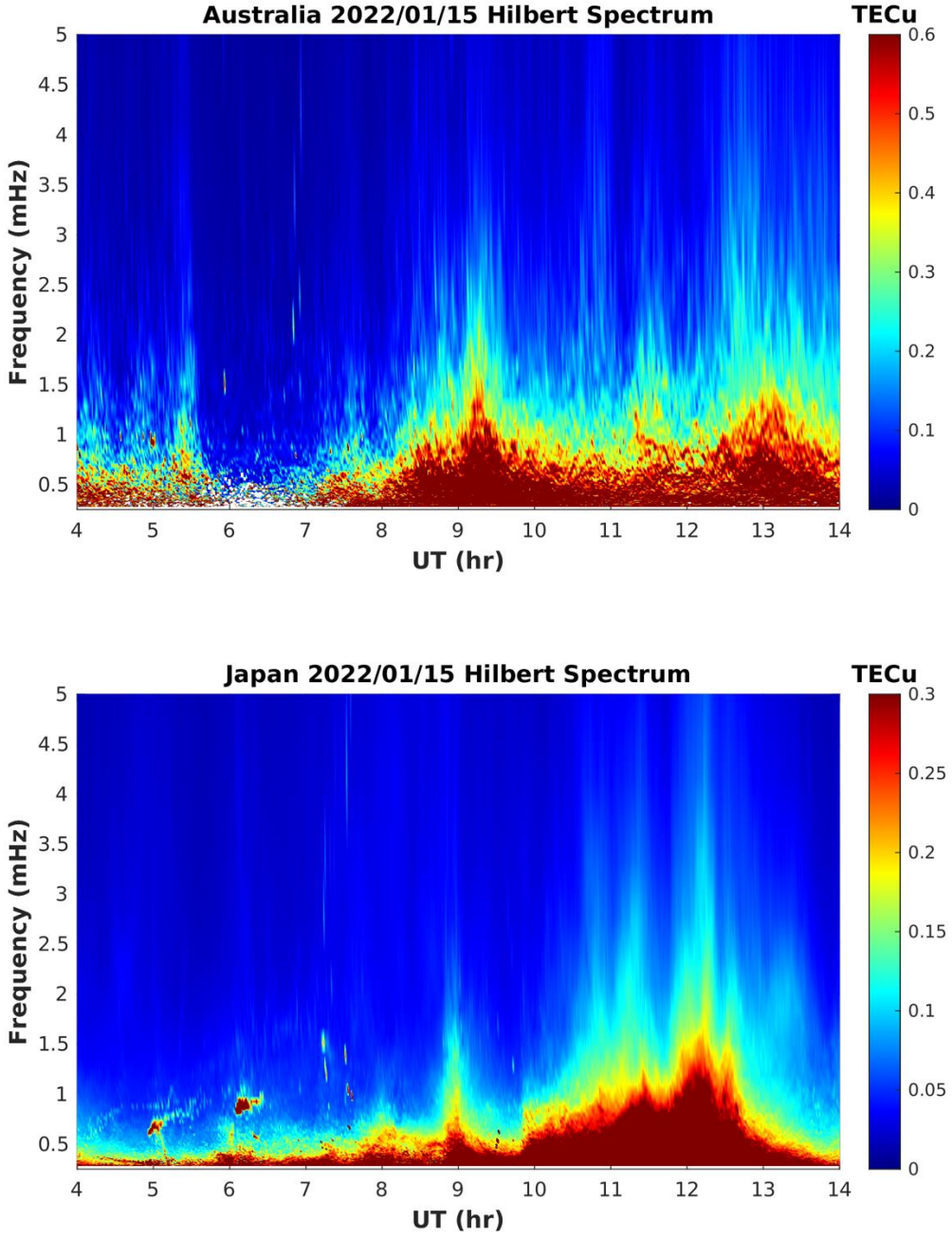


491

492 Figure 2. Hilbert Huang Transform of the TECs from Australia (top) and Japan (bottom) indicating the
493 amplitude intensification after the eruption are manifest for frequency < 2 mHz (or 500s). The amplitude
494 intensifications around 0800-1000UT for both regions suggest the conjugate effect. The minimum
495 frequency in the vertical axes is set at 0.25 mHz (or 3600s).

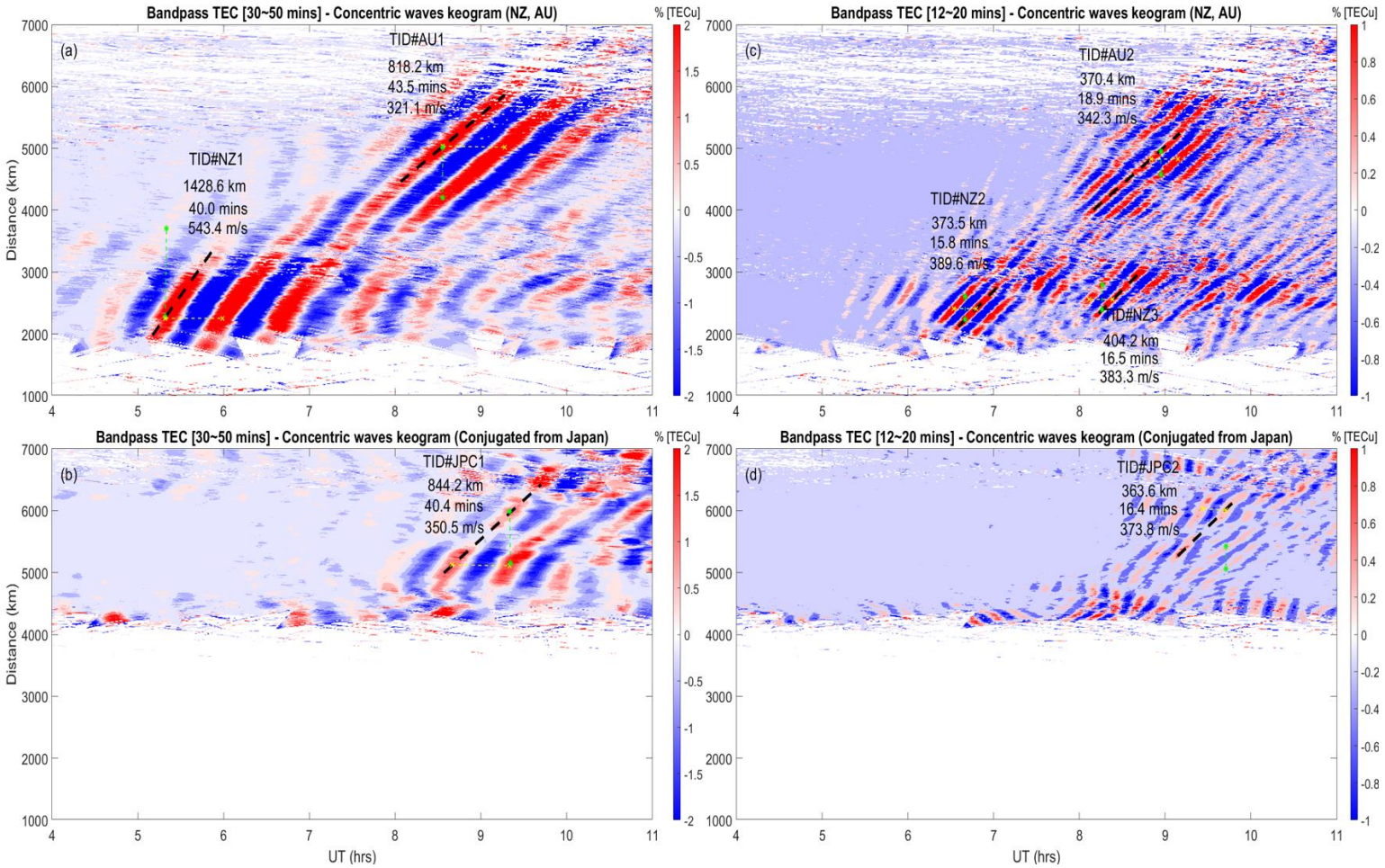


496

497 Figure 3. Keograms of the filtered TEC of 30-50 min (left) and 12-20 min (right) show the wave
498 characteristics of CTIDs after 0400UT over New Zealand-Australia in (a) and (c), as the southern
499 hemisphere conjugate locations of Japan are shown in (b) and (d). The distances are from the volcano to
500 the sub-ionospheric point (SIP) locations over New Zealand and Australia areas, as observations over
501 Japan have been mapped to the southern hemisphere.

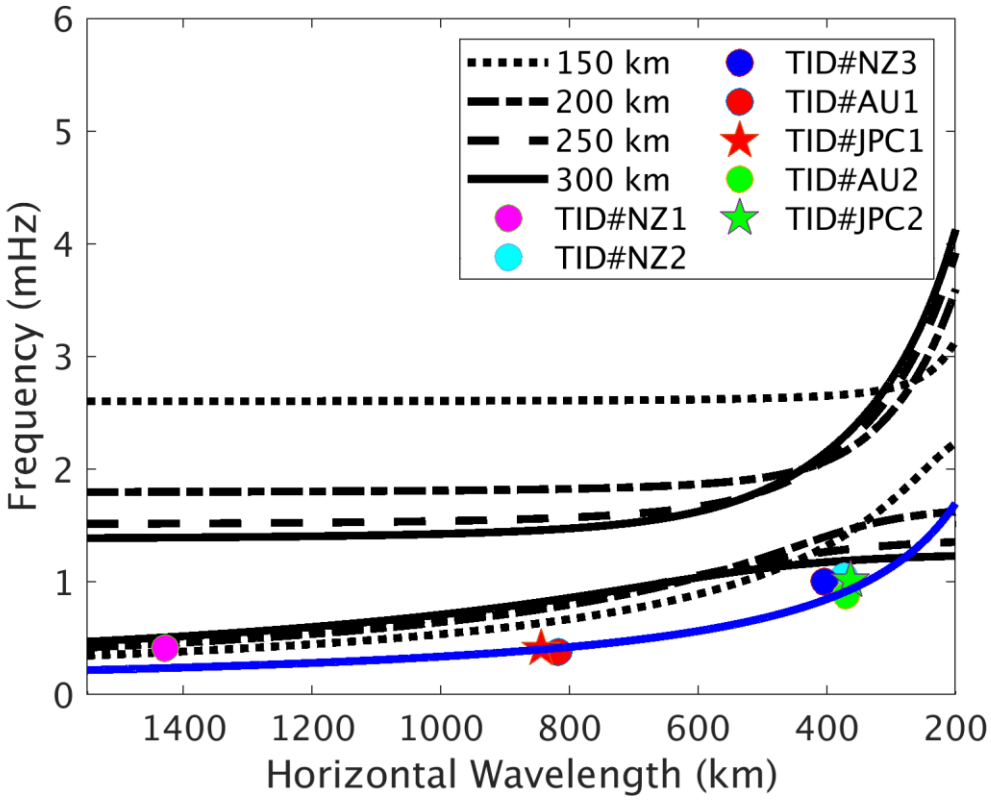


Figure 4. The theoretical dispersion curves of acoustic and gravity modes at 150 (dotted), 200 (dashed), 250 (long-dashed) and 300 (solid) km altitudes are indicated in line plots. The colored dots/asterisk correspond to the observed TIDs shown in Figure 3. Blue solid line indicates the Lamb mode.